Full Paper Transactions, SMiRT 28
Toronto, Canada, August 10-15, 2025

EFFECT OF THE WELDING PATH ON THE RESIDUAL STRESS STATE IN MULTI-PASS WELDING

Serge PASCAL[1], Rémi BOULLON[2], Thierry COUVANT[3], Diogo GONÇALVES[4]

[1] Research engineer, Univ. Paris-Saclay, CEA, SRMA, Gif-Sur-Yvette, France (serge.pascal@cea.fr)
[2] Research engineer, Univ. Paris-Saclay, CEA, SRMA, Gif-Sur-Yvette, France (remi.boullon@cea.fr)
[3] Research engineer, EDF R&D, MMC, Moret sur Loing, France (thierry.couvant@edf.fr)
[4] Research engineer, EDF R&D, MMC, Moret sur Loing, France (diogo.goncalves@edf.fr)

INTRODUCTION

The aim of this work was to study the influence of the welding path on the residual stresses of a welded component. It relies on welding simulations of two chamfered plates in butt configuration, considering two welding trajectories: one-way and back-and-forth. The modelling is based on an experimental mock-up of two 500 mm long AISI 316L(N) plates, welded in 29 passes. However, the simulation was limited to 7 passes of 100 mm length. The model was validated by comparisons to temperature and chamfer closure measurements. The main result is that the welding trajectory has a low influence on the residual stresses and cumulated plastic strain for the two welding paths investigated.

PRESENTATION OF THE WELDING MOCK-UP

The welding mock-up modelled in this works was carried out in the frame of the SiMeW (Simulation and Measurement of Welds) project, started in 2023 (Gonçalves (2023)). The welded specimens were two 316L(N) stainless steel plates of 24 mm thick, 500 mm length and 150 mm width, with an open chamfer with an internal angle of 25° (Figure 1). The chemical composition of the base (316L(N) stainless steel) and the filler (BÖHLER THERMANIT19-15) materials are detailed in Table 1.

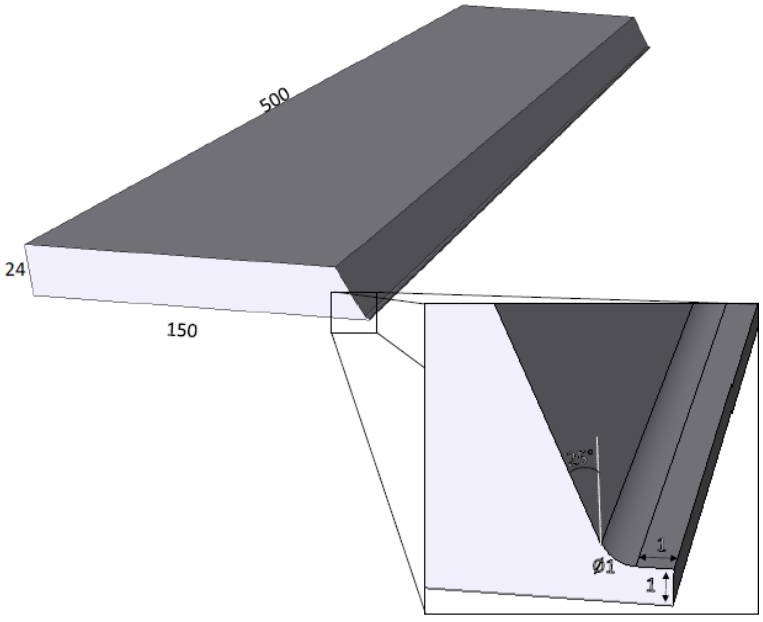

Figure 1. 316L(N) stainless steel sheets geometry (in mm), with 25° chamfer.

Table 1. Chemical composition of base (316L(N) stainless steel) and filler (19-15 stainless steel) metals.

Elements	C	N	Cr	Ni	Mo	Mn	Si	S	P	Co	Cu	B
316L(N) base metal	0.026	0.069	17.27	12.13	2.54	1.74	0.31	0.001	0.025	0.09	0.29	0.001
19-15 filler metal	<0.01	0.17	20.3	15.5	2.9	7.0	0.5	<0.01	0.01		<0.1	

The Gas Tungsten Arc Welding (GTAW) process was applied to weld the mock-up. In order to limit distortion resulting from the welding process, the steel plates were clamped using a bridge system, as shown in Figure 2. A back shielding gas is also implemented. A butt weld configuration in a flat welding position was chosen and no root gap was applied. Before welding assembly, all parts were degreased.

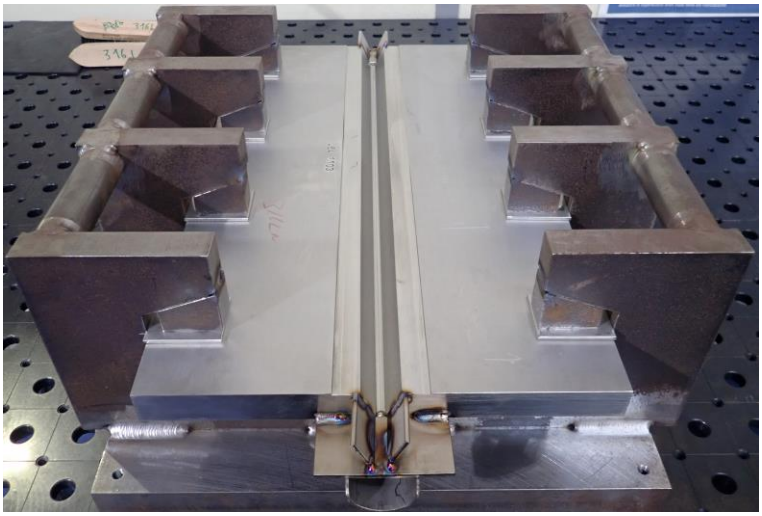

Figure 2. Steel plates clamped using a bridge system in butt weld configuration prior to welding.

Welding was achieved using a non-consumable tungsten electrode fixed above the steel plates, on an automated system enabling the welding sequence to be controlled. The 19-15 steel wire, with a diameter ϕ_w of 1 mm, arrived from the opposite direction of the welding direction, according to an angle of 65° with the electrode.

The chamfer was filled with 29 welding passes distributed over 13 layers. A diagram showing the welding sequence is presented in Figure 3. This sequence involves four types of welding pass: root (L1), support (L2), filling (L3 to L22) and finishing (L23 to L29). The welding parameters applied to each type of pass are shown in Table 2. They are the electric tension U and intensity I, the wire feed rate w_f and the welding speed s_w. The linear energy E_l is defined as UI/s_w.

Table 2. Welding parameters for the four types of welding passes.

Type	U (V)	I (A)	w_f (mm/s)	s_w (mm/s)	E_l (kJ/mm)
Root	115.0	10.0	12.5	1.0	1.15
Support	145.0	12.0	18.0	1.67	1.04
Filling	218.5	12.0	28.0	1.83	1.43
Finishing	138.5	12.0	11.25	1.67	1.0

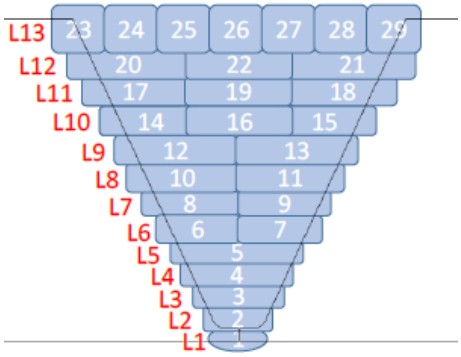

Figure 3. Diagram of the 29 welding passes distributed in 13 layers.

FINITE ELEMENT MODELLING

Finite element modelling and simulations were performed with CEA's finite element code Cast3M (2024).

Welded plate mesh

Figure 4 shows the meshes of plates (left) and weld beads (right). In the weld bead mesh, each pass is distinguished by a different color. Element size is 0.5 mm in the weld beads, as well as in the refined parts of the chamfer. For 29 welding passes, the overall mesh contains about 230,000 nodes and 232,000 elements.

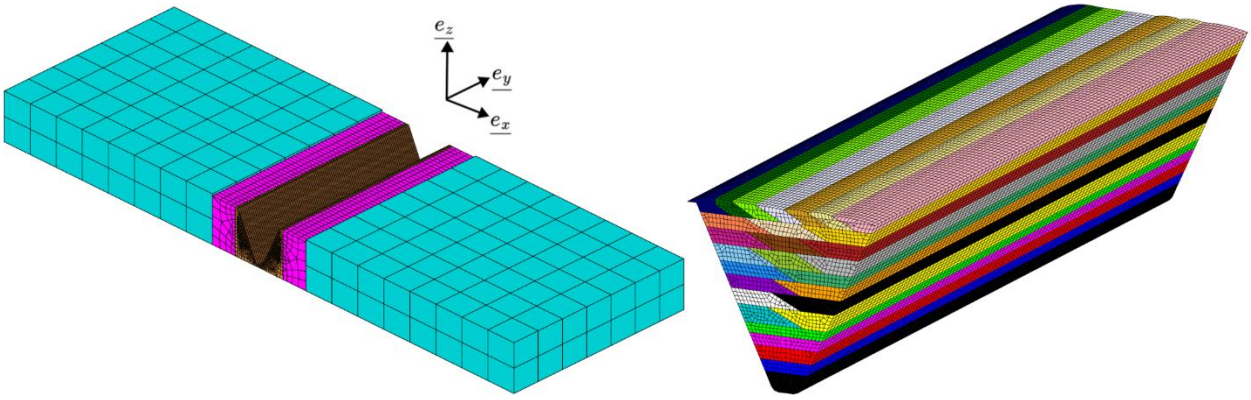

Figure 4. Meshes of plates (left) and weld beads (right), in which each welding pass has a different color.

Chamfer (in brown) and weld beads are conforming meshes. Pink, turquoise-blue and brown parts of the plate mesh have hanging nodes at their interfaces. To ensure the continuity of the solution, temperature and kinematic relations are added to the boundary conditions.

Weld beads and plates were first meshed in two dimensions, then extruded in the third dimension. The extrusion distance defines the "*mesh length*". The chamfer is meshed in one part, so the plates are supposed to be perfectly bound together, and no gaps can open up between them. Observations on the bottom side of the welded plates validated this assumption.

Filler material is deposited molten, so that its volume is expanded by the temperature. The cross-section S_b of each weld bead is consequently defined according to the welding parameters of each pass, but considering the thermal expansion:

$$S_b = \frac{\pi \phi_w^2}{4} \frac{w_f}{s_w} (1 + 2\alpha \Delta T) \quad (1)$$

In equation (1), ϕ_w, w_f, s_w are welding parameters defined previously (see Table 2), α the thermal expansion coefficient of the filler material, and ΔT the difference in temperature between ambient air and the deposited material. This assumption is validated by the fact that, if thermal expansion is not taken into account, the surface area of deposited material is not large enough to fill the cross-section of the chamfer. This means that, as each pass cools, the chamfer closes slightly, pulled in both sides by the shrinkage of the filler material.

Material deposition modelling

Material deposition is modelled by adding blocks of finite element during the simulation. The added blocks are obtained by regularly cutting the mesh of each weld bead. The blocks are about 3 mm in length. For a 100 mm long mesh, this means 33 material deposition steps per welding pass. The addition of finite element blocks is illustrated in Figure 5 with the 5th welding pass.

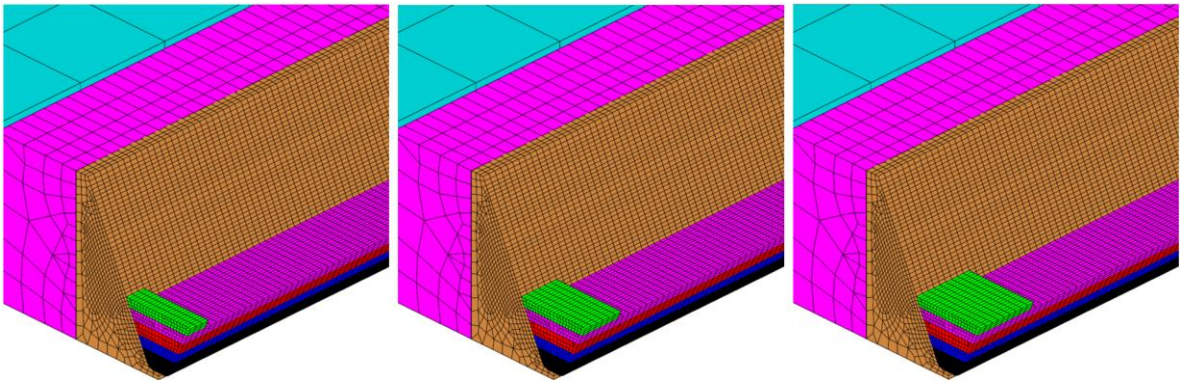

Figure 5. Illustration of material deposition with the addition of the first three finite element blocks in the 5th welding pass. Finite element blocks are about 3 mm long. In this picture, only one plate is shown to better see the weld beads.

Thermal Analysis

Nonlinear transient thermal analysis is conducted step-by-step, using an implicit first-order Euler method. During welding periods, time step is calculated to have an average of 3π time steps per finite element block addition. The added finite element blocks being about 3 mm in length for each pass, so the time step length depends on the welding speed of each pass. For the first pass, this leads to a time step of approximately 0.32 s. During cooling periods between two welding passes, time step is increased according to a geometric sequence of common ratio 2. For a simulation with a 100 mm long mesh, the simulation of 7 welding passes leads to the calculation of 2364 time steps.

AISI 316L material properties are taken from Depradeux (2004). Thermal conductivity and specific heat capacity are temperature dependent. The value of density is taken at room temperature since the analysis is conducted in the frame of small displacements. Thermal boundary conditions are convective and

radiative heat exchanges with environment. Surface of heat exchange is updated at each material deposition step to take into account the evolution of the geometry (added blocks).

Table 3 gives the values of the convective heat transfer coefficient (H_c) and material emissivity (ε), as well as the ambient air (T_a) and the initial temperatures of plates (T_p) and weld beads (T_w). When adding a finite element block, the temperature at the interface between the initial mesh and the added block is computed to satisfy energy conservation.

Table 3. Values of convective and radiative heat exchange coefficients and initial temperatures of plates and weld beads.

Parameter	$H_c\ (W/m/K)$	ε	$T_a\ (°C)$	$T_p(°C)$	$T_w(°C)$
Value	20	0.5	20	20	1800

Energy supplied by the GTAW process is modelled with a Gaussian heat source distribution $q(\vec{x})$:

$$q(\vec{x}) = q_0 \exp\left[-2\left(\frac{(x-x_s)^2+(y-y_s)^2}{R_g^2}+\frac{(z-z_s)^2}{Z_G^2}\right)\right] \quad (2)$$

In equation (2), (x_s, y_s, z_s) are the coordinates of the heat source location, R_G, Z_G the radial and axial parameters of the Gaussian distribution, respectively, and q_0 a normative parameter defined by:

$$q_0 = \frac{2^{5/2}}{\pi^{3/2}}\frac{Q_{tot}}{R_G^2 Z_G} \quad (3)$$

Such that:

$$Q_{tot} = \iiint_{Z\leq 0} q(\vec{x})dV \quad (4)$$

Q_{tot} is the power supplied by the GTAW process, which is equal to ηUI, U and I being the electric tension and intensity used in the process (see Table 2) and η its efficiency, arbitrary set to 0.9. R_G and Z_G parameters also depend on the welding pass: Z_G is equal to the pass height and R_G to half the pass width.

Mechanical Analysis

Static nonlinear analysis is performed separately, applying the temperature calculated in the thermal analysis according to the same time discretization. AISI 316L mechanical behavior is supposed to be elastoplastic, with linear kinematic hardening following the Prager's rule. Material properties are also taken from Depradeux (2004). Young's modulus, yield stress, kinematic hardening modulus and thermal expansion coefficient are temperature dependent. Poisson's ratio is taken equal to 0.3.

At high temperature, plastic hardening is annealed. Plastic annealing must be taken into account to correctly estimate the residual stresses after welding. To achieve this, the hardening variable of the elastoplastic behavior law is reset to zero when temperature exceeds a given temperature threshold T_{ann}. In the present work, T_{ann} is taken equal to $1000°C$.

Furthermore, boundary conditions need a coarse modelling of the clamping system. On the left picture in Figure 6, the grey mesh represents the bridges of the clamping system, while only the edges of the plates are shown. The nodes at the base of the bridges are embedded (red circled crosses in the picture),

while those of the clamps in contact with the top of the plates are constrained to stay perfectly bonded to these ones by applying kinematic relationships (blue circled crosses in the picture).

On the right picture in Figure 6, the green mesh strips represent the surfaces of the plates in contact with the lower support. Here again, only the edges of the plates are shown. A contact condition is prescribed to the mesh of the green surfaces ($U_z \geq 0$), while their nodes are perfectly bonded to the plate meshes by applying kinematic relationships. Finally, a condition of symmetry ($U_y = 0$) is applied to the nodes at the back of the plates in the (O, y) direction (not presented in Figure 6).

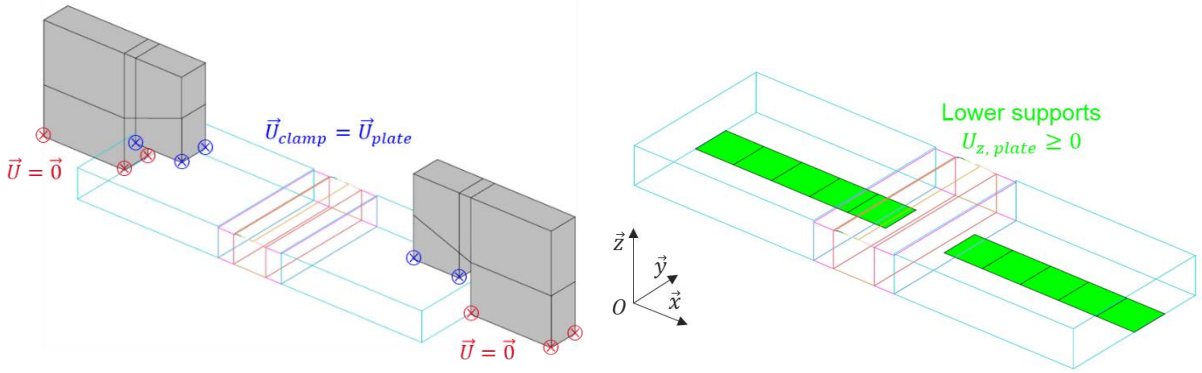

Figure 6. Boundary conditions applied to the plates and the clamping system. On the left, the grey mesh represents the bridges of the clamping system. On the right, the green mesh strips represent the surfaces of the plates in contact with the lower supports.

MODEL VALIDATION

Temperature Measurements

Temperature measurements were achieved during welding at different locations in the plates via machined holes for thermocouples. Figure 7 presents the location of the thermocouple measurements: pink and brown lines represent the edges of the central part of the plate mesh, black crosses the location of the measurements, and green dotted lines the holes drilled for the thermocouples. Note that thermocouples TC3 to TC5 and TC9 to TC11 are located at the same point on both sides of the chamfer. Note also that during the first welding passes, TC5 and TC11 are the thermocouples closest to the heat source and therefore record the highest values.

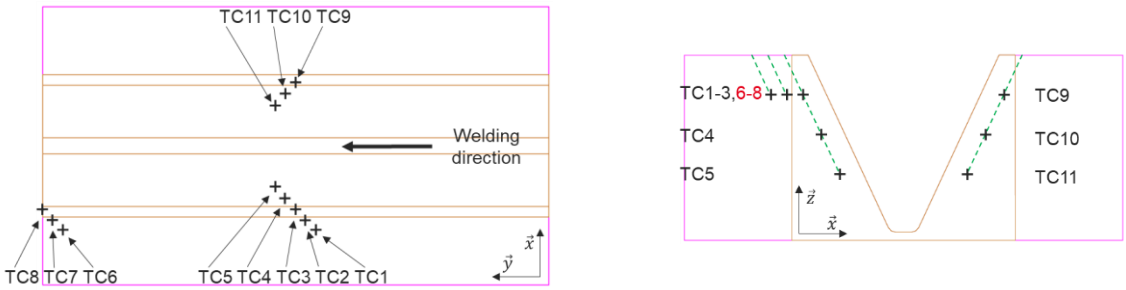

Figure 7. Locations of thermocouple measurements: top view (left) and cross section view (right) of the plate mesh.

Figure 8 presents the temperature measured by thermocouples TC1 to TC5 during the first (a) and fourth (b) welding passes, as well as the temperature calculated with the model at the same points. As can be seen, the simulation is in fairly good agreement with the measurements, although the model somewhat underestimates the temperature far from the heat source, *i.e.* for measurements at TC1 to TC3.

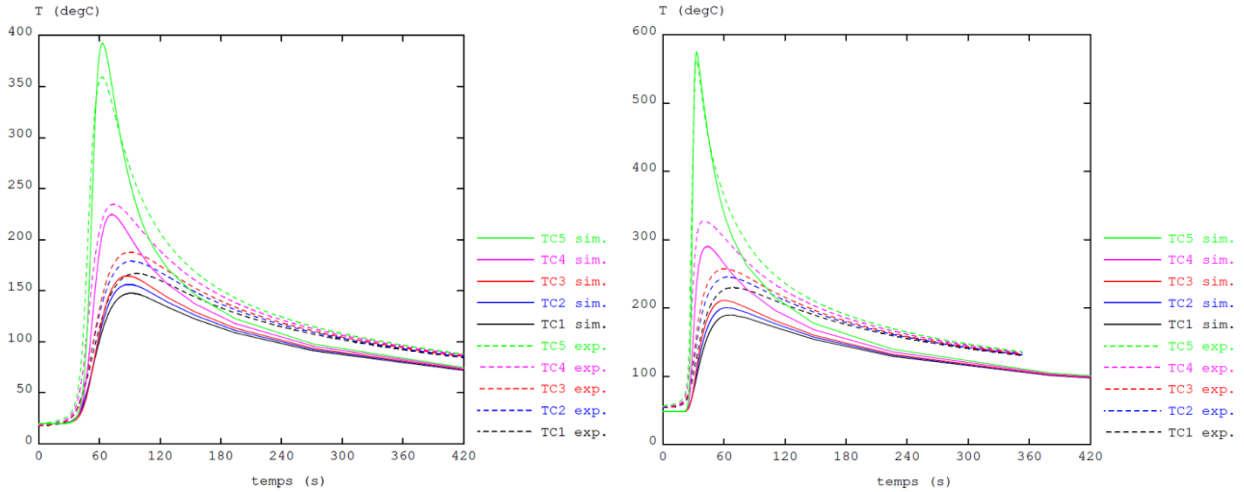

a) 1st welding pass b) 4th welding pass

Figure 8. Temperature measured by thermocouples TC1 to TC5 during the 1st (a) and 4th (b) welding passes, compared with the temperature calculated with the model at the same points.

These results were obtained after two runs of the entire thermal simulation, adjusting the heat source efficiency η from 0.8 for the first run to 0.9 for the last one. These values are consistent with the literature, see for example Collings *et al.* (1979). This result shows that heat source losses are lower at the bottom of a quite narrow chamfer than in a more open configuration, such as those encountered in the modelling of wire-arc additive manufacturing by Pascal (2022), for which the heat source efficiency was set at 0.8.

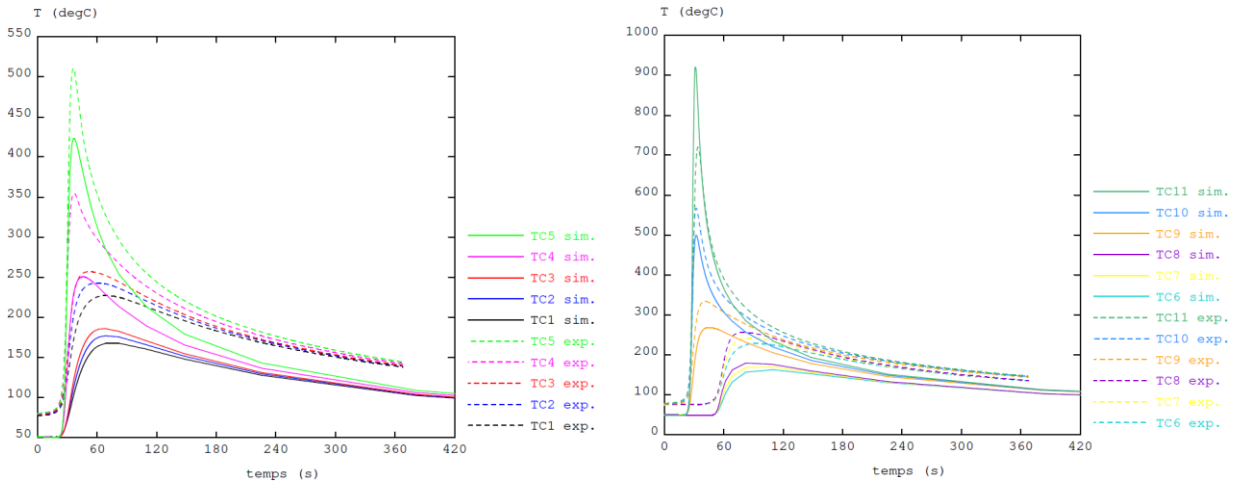

Figure 9. Temperature measured by thermocouples TC1 to TC5 (left) and TC6 to TC11 (right) during the 7th welding pass, compared with the temperature calculated with the model at the same points.

Figure 9 presents the temperature measured by thermocouples TC1 to TC5 (left picture) and TC6 to TC11 (right picture) during the 7th welding pass, compared with the temperature calculated with the model at the same points. For the 6th and 7th welding passes, the temperature field is no more symmetric between the two sides of the chamfer (see Figure 3). The 7th pass being located at the right-hand side of the chamfer, the temperature at TC11 is higher than at TC5, as well as at TC10 compare to TC4, and TC9 compare to TC3. Considering the simulation results, the temperature calculated on left-hand side of the chamfer (TC1 to TC5) is underestimated by the model, whereas temperature calculated on right-hand side is overestimated (TC9 to TC11). These results highlight that the radius of the Gaussian distribution should be increased in order to balance the maximum of temperature between the two sides of the chamfer.

Chamfer Closure

The evolution of the chamfer width was experimentally measured. Figure 10 compares the change in chamfer width for each welding pass for the one-way path (left) and the back-and-forth path (right) with these experimental measurements. As can be seen, the simulation (red solid lines) does not match the experimental measurements (green and blue dotted lines). This difference can be explained by the sliding of the plates under the clamping bridges, which is not modelled in the current simulation, which assumes a perfect bond between the two parts.

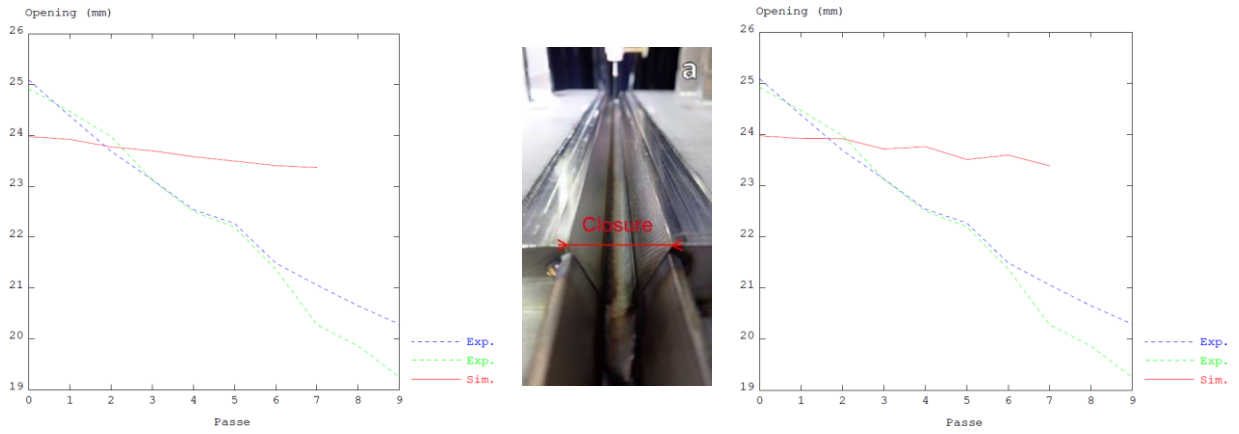

Figure 10. Change in chamfer width for each welding pass for the two welding paths: one-way (left) and the back-and-forth (right). Dotted lines represent experimental measurements, whereas red solid lines represent simulation results.

EFFECT OF THE WELDING PATH ON MECHANICS

During Welding

Figure 11 compares the contour plot of the von Mises stress field in one plate and the beads during the 5th pass when welding along a one-way path (left) or a back-and-forth path (right). As can be seen, there is a small difference between these two pictures. Contour plots of the stress components at different moments of the welding show the same trend, as similarly does the accumulated plastic strain. Finally, the welding trajectories have a low influence on the mechanical state of the plates during welding, at least for the two paths investigated here.

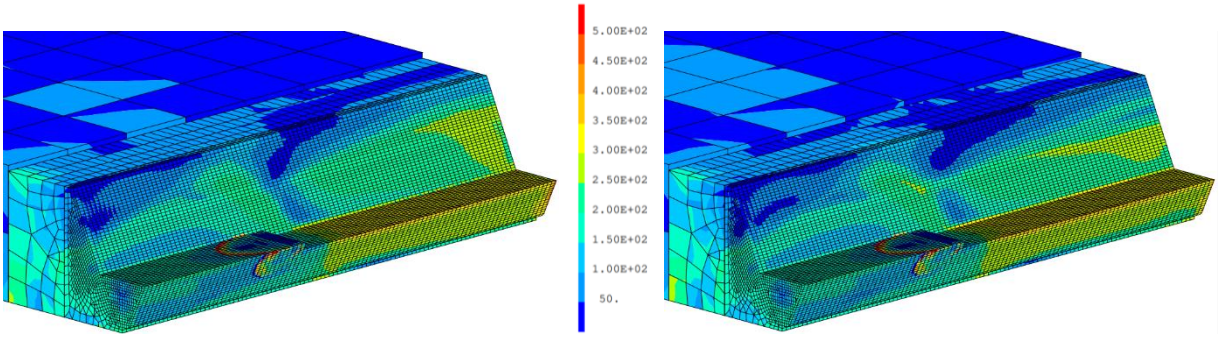

Figure 11. Contour plot of the von Mises stress field in one plate and the beads during the 5th pass when welding according to a one-way path (left) or a back-and-forth path (right).

After Welding and Cooling

Figure 12 presents the contour plot of the σ_{xx} component of the stress field in one plate and the beads after cooling for the two welding paths. Here again, there is a small difference on the residual stress field generated by the welding for the 2 paths investigated. Unclamping has not been simulated but the conclusion would be the same since it only involves a spring-back in the component. The comparison of the cumulated plastic strain obtained for the 2 welding paths leads to the same conclusion (Figure 13).

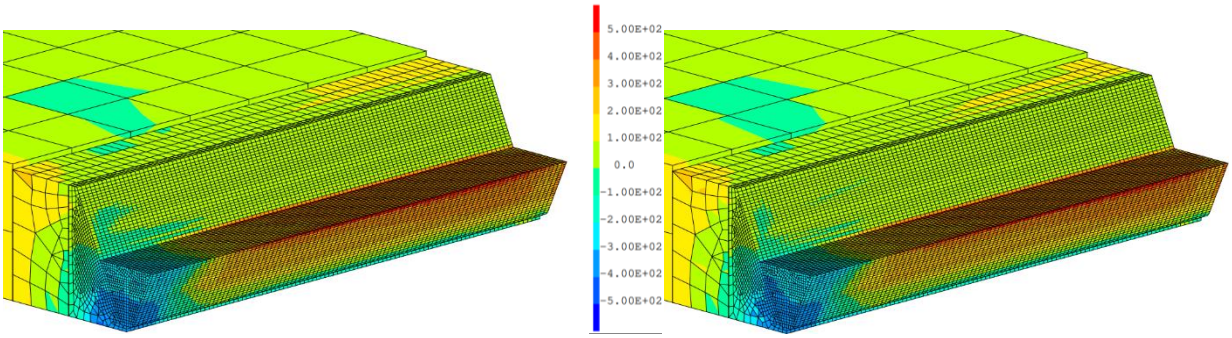

Figure 12. Contour plot of the σ_{xx} component of the stress field in one plate and the beads after cooling for the two welding paths: one-way (left) and back-and-forth (right).

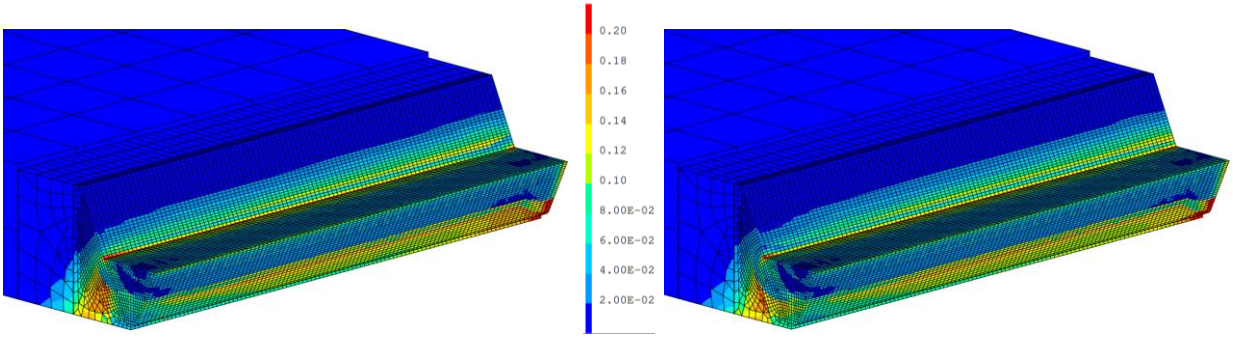

Figure 13. Contour plot of the cumulated plastic strain in one plate and the beads after cooling for the two welding paths: one-way (left) and back-and-forth (right).

CONCLUSIONS

The aim of this work was to study the influence of the welding path on the residual stresses of a welded assembly. It is based on welding simulations of two chamfered plates in butt configuration, considering two welding trajectories: one-way and back-and-forth. The modelling is based on an experimental mock-up of two 500 mm long AISI 316L plates, welded in 29 passes. However, the simulation was limited to 7 passes of 100 mm length.

The model was validated by experimental comparisons to temperature and chamfer closure measurements. Thus, model calibration had only two runs of simulation. On one-hand, temperature comparisons showed a good agreement of the simulation to experimental data, even though heat source radial distribution should be somewhat increased to better balance the maximum of temperature between the two sides of the chamfer. On the other hand, comparisons on the chamfer closure showed that the model did not match the measurements. The difference can be explained by the plates sliding under the clamping bridges, whereas the model assumes a perfect bonding between the two parts. Frictional contact should be introduced into the modelling to better represent the boundary conditions of the clamping system.

Comparisons carried out on results obtained using two welding paths showed a small difference in stress fields and accumulated plastic strain. In conclusion, the welding trajectory does not appear to have a significant effect on the residual stresses of the welded component for the two welding paths investigated.

REFERENCES

Cast3M (2024), CEA, https://www-cast3m.cea.fr

Collings, N., Wong, K. and Guile, A. (1979). “Efficiency of tungsten-inert-gas arcs in very-high-speed welding”, *Proc. of the Institution of Electrical Engineers*, vol. 126, pp. 276–280, IET.

Depradeux, L. (2004). “*Simulation numérique du soudage - Acier 316L: validation sur cas tests de complexité croissante*”. Doctoral thesis, Institut National des Sciences Appliquées de Lyon.

Gonçalves, D. (2023). *SiMeW project, Deliverable D1.1: Manufacturing of 316LN stainless steel GTAW mock-ups*, CEA technical report, DES/ISAS/DRMP/SRMA/LTA/NT/2023-031.

Pascal, S. and Gounand, S. (2022). “Modélisation thermomécanique d’un cas d’étude de fabrication additive arc-fil”, *Proc. 15ième colloque national en calcul des structures*, Université Polytechnique Hauts-de-France, Hyères-les-Palmiers, France.